# Pseudo Training Data Generation for Unsupervised Cell Membrane Segmentation in Immunohistochemistry Images

Xi Long[1,*], Tianyang Wang[1,*], Yanjia Kan[1,*], Yunze Wang[1], Silin Chen[2], Albert Zhou[3], Xianxu Hou[1], Jingxin Liu[1†]

[1]Xi'an Jiaotong-Liverpool University, School of AI and Advanced Computing, Suzhou, China
[2]Beijing Jiaotong University, School of Mathematics and Statistics, Beijing, China
[3]University of Warwick, UK

*Abstract*—In the realm of clinical diagnostics and medical research, quantitative assessment of membrane activity in immunohistochemistry (IHC) images is standard practice. Despite a high demand for cell membrane segmentation, only a few algorithms have been developed, and there is a lack of open datasets in this field. In this paper, we propose a three-stage unsupervised framework to accurately segment positive cell membranes in IHC images. Our approach transforms the unsupervised segmentation task into a supervised one by generating pseudo-paired training data using Voronoi diagrams and CycleGAN. Additionally, we introduce a dual encoder segmentation model with domain adaptation modules to mitigate the domain shift between generated images and real images. To our best knowledge, this is the first work focusing on unsupervised learning for IHC cell membrane segmentation. Extensive experiments and ablation studies on our newly built IHC cell membrane segmentation dataset validate the effectiveness of our framework.

*Index Terms*—Histopathology, Immunohistochemistry, Membrane Segmentation, Unsupervised Semantic Segmentation

## I. INTRODUCTION

Immunohistochemistry (IHC) is a fundamental technique widely employed in both medical research and clinical diagnostics. By utilizing monoclonal and polyclonal antibodies, IHC facilitates the visualization and quantification of specific proteins within tissues, including those located on cell membranes, exemplified by the majority of CD antigens (i.e., HER2, PD-L1, CD30, etc.) [1], [2]. With the ongoing advancements in precision diagnosis and immunotherapy, there is a pressing need for precise interpretation of IHC, highlighting the crucial role of expertise in this domain.

Given the recent advances in the field of computer vision, an increasing number of clinicopathologic Computer-Aided Diagnosis (CAD) systems are being developed to assist pathologists in providing precise quantitative information [3]–[7]. The accurate segmentation of positively stained cell membranes represents a key step in analyzing membrane-stained IHC sections [8]–[11]. Despite the considerable demand for cell membrane segmentation, only a limited number of algorithms have been developed for this purpose.

Early algorithms primarily utilize image processing techniques due to the distinct appearance of the positively stained

cell membrane, which typically exhibits a crisp brown colour, contrasting sharply with the achromatous negative cell membrane and the blue nucleus. [12] and [13] proposed employing Support Vector Machines (SVM) to classify pixels into brown staining and others, whereas colour deconvolution [14] followed by a series of post-processing steps proposed in [9] to segment the positive membrane. To recognize the entire cell membrane, [15] first detected the nucleus and then used nuclear membranes as a spatial reference to reconstruct the unstained tracts. Traditional methods, less reliant on precise annotations, struggle with complex situations like noise from overlapping and diffusing stains in pathology images. They are inefficient when using color thresholds for pixel classification or membrane segmentation in such noisy conditions.

Several studies have explored deep learning methods for cell membrane segmentation. Khameneh et al. [16] combined an SVM classifier to identify regions of interest (ROIs) with a U-net model for more accurate membrane region segmentation. Saha et al. [17] introduced a long short-term memory (LSTM) architecture for detecting cell membranes and nuclei, while an active learning-based technique was proposed by Gaur et al. [18]. However, these methods typically require extensive annotations, which are labour-intensive and challenging to acquire.

In this paper, we propose a three-stage unsupervised framework for accurately segmenting the positive cell membrane in IHC images, achieved by generating a pseudo-paired training set and domain adaptive segmentation model. Specifically, we first use random membrane structure images generated by Voronoi diagrams and randomly sampled IHC patch images to generate pseudo-paired data via CycleGAN [19]. Inspired by [20], we introduce *YNet* for membrane segmentation, which employs two encoders to handle low-frequency (LF) and high-frequency (HF) images through wavelet transformation, along with the dual domain adaptation module to address artificial perturbations from generated images. To the best of our knowledge, this is the first unsupervised semantic segmentation framework on immunohistochemical cell membrane images. The contribution of this work is three-fold:

- We present an unsupervised framework comprising three stages for cell membrane segmentation in IHC images;

---
*: Equal Contribution; †: Corresponding Author.

- We introduce a novel segmentation model named *YNet*, which employs wavelet transformation to produce low-frequency (LF) and high-frequency (HF) images as inputs. Additionally, *YNet* incorporates a domain adaptive module for each frequency component to counteract the domain shift between generated data and real data.
- We evaluate the efficacy of our proposed framework through comprehensive experiments on a new IHC cell membrane segmentation dataset , demonstrating substantial improvement over existing methods.

## II. METHOD

The overview of our proposed framework is illustrated in Fig. 1. It consists of three stages of membrane curvilinear image generation, pseudo-paired data generation, and membrane segmentation model. In the first stage, membrane curvilinear images are generated. These, along with real IHC image patches, are used as inputs in the second stage. Finally, the segmentation model is trained using the pseudo-paired data generated in the second stage.

### A. *Membrane Curvilinear Image Generation*

The voronoi diagram is a geometric structure that divides space into regions, each region is determined by its nearest generated point, ensuring that any point within it is closer to its centre point than to other generated points [21]. Mathematically, the Voronoi diagram is defined by a set of generating points and the regions they create. Let $P = \{p_1, p_2, ..., p_n\}$ be a set of $n$ distinct points in a space $S$, where the number of seed points, $n$, is randomly chosen from the interval $(90, 120)$, primarily based on the density we observe in real IHC images to better match the real image distribution. The Voronoi region $V(p_i)$ associated with each point $p_i$ is defined as the set of all points $x$ in $S$ whose distance to $p_i$ is less than or equal to its distance to any other point $p_j$ in $P$. This can be formally expressed as:

$$V(p_i) = \{x \in S \mid \|x - p_i\| \leq \|x - p_j\| \text{ for all } p_j \in P, j \neq i\} \tag{1}$$

where $\|x - p_i\|$ denotes the distance between the point $x$ and the generated point $p_i$. The Voronoi diagram $\text{VD}(P)$ of the set of points $P$ is the collection of all Voronoi regions $V(p_i)$ with each point $p_i$ in $P$. This can be expressed as:

$$\text{VD}(P) = \{V(p_1), V(p_2), ..., V(p_n)\} \tag{2}$$

The Voronoi diagram $\text{VD}(P)$ of a point set $P$ in a two-dimensional space S is partitioned by the vertical bisector of each point $p_i$. These bisectors define the region $V$ of $p_i$ centered at $p_i$, which contains all points that are at distance $p_j$ or less than $p_i$. In essence, the Voronoi diagram consists of a series of equidistant regions centred at each point in the point set $P$.

**Natural perturbations.** To enhance the realism and complexity of biological cell membranes, we have augmented the traditional Voronoi diagram with natural perturbations. These perturbations introduce subtle irregularities into the Voronoi

cell boundaries by incorporating controlled random noise into the coordinates of the seed points. The perturbation is defined as follows:

$$p_i' = p_i + \epsilon, \quad \epsilon \sim \mathcal{N}(0, \sigma^2) \tag{3}$$

where $p_i'$ denotes the coordinates of the seed points after perturbation. The noise $\epsilon$ is sampled from a normal distribution $N(0, \sigma^2)$. The standard deviation $\sigma$ is chosen from the range $(0.005, 0.01)$.

**Edge preservation.** To mimic the discontinuous and irregular edges of cell membranes, we propose a heuristic for selective edge preservation. Instead of keeping all Voronoi edges, we randomly delete a portion based on a specified edge retention rate within $(0.6, 1.0)$. This diversifies the Voronoi diagram and simulates the membrane's discontinuities and irregular edges.

**Smooth curve and random line width.** To simulate cell membrane contours, we integrate conic curves into the enhanced Voronoi diagram, creating smoother shapes between adjacent points. In addition, considering the non-uniform thickness of biological cell membranes, we randomly select curve widths ranging from $(1, 5)$ to mimic thickness and morphology variations. Further, we enhance realism through colour mapping.

### B. *Pseudo-Paired Data Generation*

**Motivation.** In the previous section, we generate curvilinear structures resembling cell membranes using Voronoi diagrams. While these structures are morphologically similar to real cell membranes, they lack the realistic texture and colour style found in histopathology images. To address this limitation, we choose a classic and effective tool, CycleGAN [19], to migrate style from real pathology images to Voronoi diagram-generated ones (Fig. 1 (b)). CycleGAN is particularly well-suited for this task due to its ability to perform unpaired image-to-image translation, effectively learning the mapping between the generated and real images. This enables the creation of pseudo-pathology images, which can be used as paired data for subsequent semantic segmentation models.

**Style transfer process.** We leverage the CycleGAN framework to perform style transfer. CycleGAN operates by training two generators, denoted as $G : X \rightarrow Y$ and $F : Y \rightarrow X$, where $X$ represents the domain of Voronoi diagram-generated images and $Y$ represents the domain of real pathology images. Additionally, it trains two discriminators, $D_X$ and $D_Y$, which are responsible for distinguishing between source and translated images. To train CycleGAN, the adversarial loss is used to achieve the domain transfer as follows:

$$\mathcal{L}_{\text{GAN}}(G, D_Y, X, Y) = \mathbb{E}_{y \sim p_{\text{data}}(y)}[\log D_Y(y)] \\ + \mathbb{E}_{x \sim p_{\text{data}}(x)}[\log(1 - D_Y(G(x)))] \tag{4}$$

$$\mathcal{L}_{\text{GAN}}(F, D_X, Y, X) = \mathbb{E}_{x \sim p_{\text{data}}(x)}[\log D_X(x)] \\ + \mathbb{E}_{y \sim p_{\text{data}}(y)}[\log(1 - D_X(F(y)))] \tag{5}$$
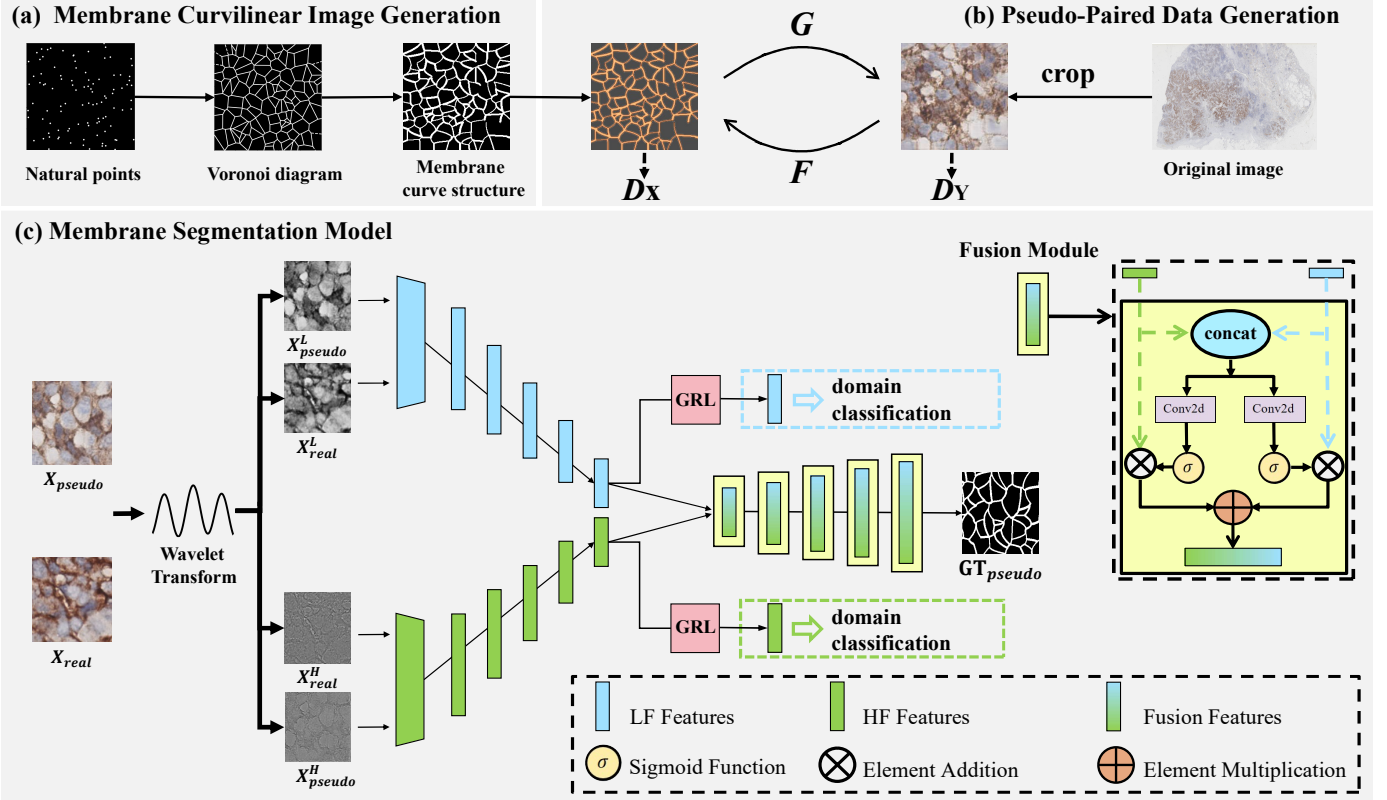
Fig. 1: Overview of our framework, which consists of three stages: (a) *Membrane Curvilinear Image Generation*: generating membrane structure image as the input of (b); (b) *Pseudo-paired Data Generation*: generating paired training data for (c); (c) *Membrane Segmentation Model*: the semantic segmentation model for the positive cell membrane segmentation.

where $\mathcal{L}_{\text{GAN}}(G, D_Y, X, Y)$ represents the adversarial loss function for the generator $G$ and discriminator $D_Y$, aiming to train $G$ to generate images indistinguishable from real images in domain $Y$, and $D_Y$ to correctly distinguish between real images from domain $Y$ and those generated by $G$ from domain $X$. Similarly, $\mathcal{L}_{\text{GAN}}(F, D_X, Y, X)$ represents the adversarial loss function for the training from domain $Y$ to domain $X$.

In addition to the adversarial losses, we also incorporate a cycle consistency loss as follows:

$$\mathcal{L}_{\text{cyc}}(G, F) = \mathbb{E}_{x \sim p_{\text{data}}(x)}[|F(G(x)) - x|_1] \\ + \mathbb{E}_{y \sim p_{\text{data}}(y)}[|G(F(y)) - y|_1] \quad (6)$$

### C. Membrane Segmentation Model

In this section, we introduce a novel *YNet* model, as depicted in Fig. 1 (c). Initially, we apply a wavelet transformation to decompose the input image into its high-frequency and low-frequency components. We then utilize two separate encoders to extract features from these components. Furthermore, we employ a decoder to fuse the features from both frequencies, to produce the final segmentation. Finally, two domain adaptive modules are used to align the features extracted from pseudo (generated) and real cell membrane images.

**Wavelet transform.** As illustrated in Fig. 2, we first employ wavelet transformation [22] to decompose raw images into low-frequency (LF) and high-frequency (HF) components of

the IHC images, which helps in accurately identifying edges and textures. As illustrated in Fig. 1, we denote the low-frequency components for the pseudo and real membrane cell images as $X_{pseudo}^L$ and $X_{real}^L$, respectively. Similarly, $X_{pseudo}^H$ and $X_{real}^H$ represent the corresponding high-frequency components. We represent LF images as $L$ and HF images as $H$, where $H$ is the sum of the horizontal, vertical, and diagonal HF components after normalization. $L$ and $H$ are defined as:

$$\begin{cases} L = LL \\ H = HL + LH + HH \end{cases} \quad (7)$$

**Encoder.** As shown in Fig. 1 (c), we utilize two distinct encoders to separately extract features from the low-frequency and high-frequency components of input images. These encoders share the same architecture but are trained with different weights. Each encoder comprises five convolutional blocks, with a reduction in feature size and a doubling of channel dimension after each block.

**Fusion module.** Inspired by the LSTM's integration of historical and current features, we adopt a similar gating mechanism to fuse low-frequency and high-frequency features:

$$O = \sigma(Conv(H, L); \theta_H)) \cdot H + \sigma(Conv(H, L); \theta_L)) \cdot L \quad (8)$$

where $O$ is the merging feature used for decoder, $Conv$ is convolution operation, $\theta_H$ and $\theta_L$ is trainable parameter for the convolution operation.
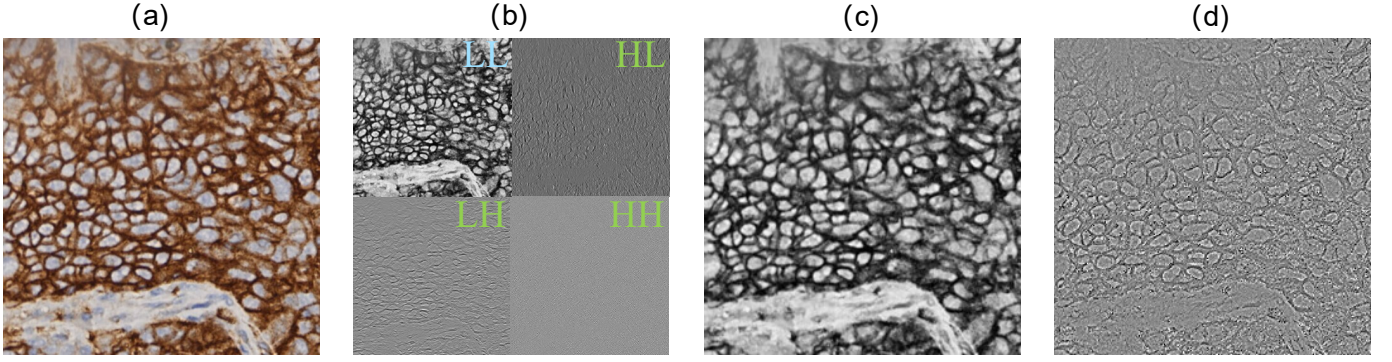
Fig. 2: **Visualization of Wavelet Transform.** (a) Original IHC image showing detailed cell membranes with intense staining; (b) Sub-band images of the wavelet transform: LL (low-frequency component), HL (horizontal high-frequency component), LH (vertical high-frequency component), and HH (diagonal high-frequency component); (c) LL image highlighting overall structural features; (d) Composite H image derived by summing normalized HL, LH, and HH components to emphasize fine details.

**Decoder.** Our decoder obtains the final segmentation by merging the features extracted from both the low-frequency and high-frequency components. Following the U-Net framework [23], we concatenate the corresponding features from the encoder to the decoder. During training, the cross-entropy loss is calculated as follows:

$$\mathcal{L}_{seg} = \mathcal{L}_{cls}(\hat{y}, y) \tag{9}$$

where $\hat{y}$ represents the predicted logits and $y$ is the labels from $\mathbf{GT}_{pseudo}$.

**Feature alignment.** In our framework, pseudo-pair images are used for supervised segmentation training. Nevertheless, the domain gap between the generated fake images and the real images presents a challenge. To align the encoded features from both the fake and real images, we utilize a domain adaptive module equipped with a Gradient Reversal Layer (GRL) [24] at the end of each encoder. Note that we perform the feature alignment for both low-frequency and high-frequency branches. We formulate the binary classification loss as:

$$\mathcal{L}_{align} = \mathcal{L}_{cls}(\hat{y}^H, y^H) + \mathcal{L}_{cls}(\hat{y}^L, y^L) \tag{10}$$

where $\hat{y}^H$ and $\hat{y}^L$ represent the predicted logits of the domain classifier for the high-frequency and low-frequency branches, respectively. $y^H$ and $y^L$ are the corresponding domain labels.

**Overall training objective.** The overall loss can be formulated as:

$$\mathcal{L} = \mathcal{L}_{seg} + \alpha\mathcal{L}_{align} \tag{11}$$

where $\alpha$ is the hyper-parameter to balance the two losses.

## III. EXPERIMENTS AND RESULTS

### A. Dataset

We introduce the IHC Membrane Segmentation (IHC-MS) dataset, which consists of 205 image patches from Immunohistochemistry (IHC) staining. Each image with 500 × 500 resolution, was extracted from 11 lung squamous cell carcinoma Whole Slide Images (WSIs) stained for programmed cell death-1 (PD-1) at 20× optical magnification (0.475μm/pixel). The positive stain membranes in these images were manually annotated by two trained students and verified by two experienced pathologists. As our proposed framework operates in an entirely unsupervised manner, all images in the IHC-MS dataset are designated for use in the test set.

### B. Implementation Details

We generate 5000 pseudo-labeled masks using Voronoi Diagrams and train a CycleGAN using these masks along with an equal number of real IHC image patches. During the training of *YNet*, we also use these 5000 real images for domain adaptation. Both CycleGAN and *YNet* are trained using the AdamW optimizer [25] with a learning rate of $1e^{-4}$.

### C. Results

We benchmark our framework against two traditional image processing-based methods such as Color Deconvolution (CD) [14] and the positive membrane detection module (PMD) introduced in [9], as well as two deep learning-based models, CycleGAN and Pix2Pix. For CycleGAN, we utilize our trained model to generate segmentation results for the stained membrane images in our test dataset. For Pix2Pix [26], we train the model using our pseudo-paired dataset.

We report the segmentation results using the Dice Coefficient [27], Hausdorff Distance [28] and Accuracy in Table I. Our model achieved a Dice Coefficient of 52.15%, outperforming both traditional methods (CD at 43.40% and PMD at 48.09%) and generative adversarial network-based approaches (CycleGAN at 43.58% and Pix2Pix at 42.80%). Moreover, our approach significantly reduced the Hausdorff Distance to 46.69, suggesting that it not only accurately segments the membrane but also ensures a closer alignment to the true membrane boundaries compared to other methods. Our framework also excelled in overall accuracy, reaching 81.42%. Notably, the comparative methods require threshold settings for their segmentation process. To ensure fairness and optimize their performance, we conduct multiple rounds
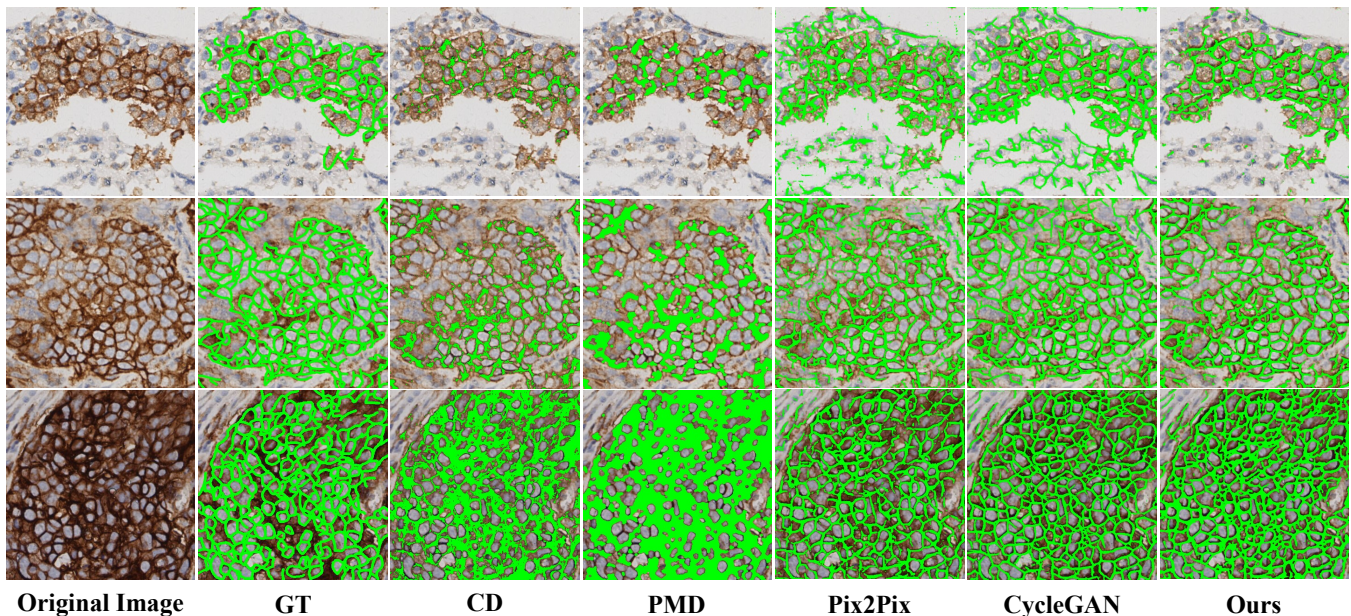
Fig. 3: Qualitative results of cell membrane segmentation on three different stain intensity images.

TABLE I: Comparison with state-of-the-art methods for unsupervised positive membrane segmentation on the new dataset IHC-MS.

|  | Method | DICE (%) ↑ | Hausdorff Distance ↓ | Accuracy (%) ↑ |
|---|---|---|---|---|
| Traditional | CD [14] | 43.40 | 61.42 | 80.63 |
|  | PMD [9] | 48.09 | 62.02 | 80.94 |
| Generative | Pix2Pix [26] | 42.80 | 54.35 | 74.38 |
| Adversarial | CycleGAN [19] | 43.58 | 59.87 | 74.16 |
| **Unsupervised** | **Ours** | **52.15** | **46.69** | **81.42** |

of testing, adjusting the thresholds accordingly. The results presented in Table I represent the best outcomes obtained for each method during our comprehensive assessment. It can be observed that our framework surpasses all other methods by a considerable margin on all evaluation metrics. The PMD achieves a higher Dice score compared to CycleGAN and Pix2Pix, but it exhibits notably poorer performance on the Hausdorff distance metric. Qualitative results in Figure 3 show that deep learning-based algorithms demonstrate more accurate membrane segmentation, and our approach exhibits superior performance in both positive and negative areas.

### D. Ablation Study

In comparison to CycleGAN, we have validated the indispensability of the individual segmentation module. We further conduct an ablation study to underscore the necessity of the two modules within *YNet*, i.e., the wavelet transform and the domain adaptive module. As shown in Table II, adding the domain adaptive module improves the performance of all models, demonstrating its effectiveness. While utilizing either high-frequency or low-frequency input alone results in inferior performance compared to the original RGB image with a single encoder, the combination of both inputs through the

TABLE II: Ablation on the effectiveness of various components, including LF images, HF images and domain adaptive module.

| Raw | LF | HF | GRL | DICE (%) ↑ | Hausdorff Distance ↓ |
|---|---|---|---|---|---|
| ✓ |  |  |  | 47.57 | 57.51 |
| ✓ |  |  | ✓ | 48.87 | 53.08 |
|  | ✓ |  |  | 49.37 | 49.06 |
|  | ✓ |  | ✓ | 51.49 | 49.00 |
|  |  | ✓ |  | 43.53 | 116.96 |
|  |  | ✓ | ✓ | 27.35 | 98.68 |
|  | ✓ | ✓ |  | 51.10 | 55.07 |
|  | ✓ | ✓ | ✓ | **52.15** | **46.69** |

TABLE III: Analysis of the Hyper-Parameter $\alpha$ on Segmentation Performance Metrics

| Hyper-Parameter $\alpha$ | DICE (%) ↑ | Hausdorff Distance ↓ | Accuracy (%) ↑ |
|---|---|---|---|
| 0 | 51.10 | 55.07 | 80.87 |
| 0.1 | 46.25 | 58.32 | 80.19 |
| **0.5** | **52.15** | **46.69** | **81.42** |
| 1 | 51.95 | 49.49 | 81.15 |

dual-encoder architecture yields superior results compared to the single-path model. Additionally, we explore the impact of the hyper-parameter $\alpha$ as detailed in Table III, which balances the segmentation loss with the domain adaptation loss, on the overall performance of our model. We discover that setting $\alpha = 0.5$ is optimal, yielding the highest performance in all metrics.

### IV. CONCLUSIONS

In this paper, we study the unsupervised cell membrane segmentation on IHC stained histopathology images. Our proposed framework tackles the unsupervised challenge by

transforming it into a supervised task through the generation of paired training data, followed by the implementation of domain adaptive *YNet* to mitigate artificial perturbations inherent in the generated data. Our method demonstrates promising results compared to existing unsupervised approaches. We anticipate that our approach will contribute to advancements in unsupervised semantic segmentation and hold potential to improve the accuracy of clinical diagnoses in real-world scenarios.

## REFERENCES

[1] S. A. Pileri, G. Roncador, C. Ceccarelli, M. Piccioli, A. Briskomatis, E. Sabattini, S. Ascani, D. Santini, P. P. Piccaluga, O. Leone *et al.*, "Antigen retrieval techniques in immunohistochemistry: comparison of different methods," *The Journal of Pathology: A Journal of the Pathological Society of Great Britain and Ireland*, vol. 183, no. 1, pp. 116–123, 1997.

[2] M. S. Tuffaha, H. Guski, G. Kristiansen, M. S. Tuffaha, H. Guski, and G. Kristiansen, *Immunohistochemistry in tumor diagnostics*. Springer, 2018.

[3] I. Kim, K. Kang, Y. Song, and T.-J. Kim, "Application of artificial intelligence in pathology: Trends and challenges," *Diagnostics*, vol. 12, no. 11, p. 2794, 2022.

[4] K. You, S. Lee, K. Jo, E. Park, T. Kooi, and H. Nam, "Intra-class contrastive learning improves computer aided diagnosis of breast cancer in mammography," in *International Conference on Medical Image Computing and Computer-Assisted Intervention*. Springer, 2022, pp. 55–64.

[5] X. Feng, Q. Shen, C. Li, X. Wang, N. Xie, L. Xie, Y. Fang, and Z. Wu, "A privacy preserving computer-aided medical diagnosis framework with outsourced model," in *2023 IEEE International Conference on Bioinformatics and Biomedicine (BIBM)*. IEEE, 2023, pp. 1080–1087.

[6] K. Doi, "Computer-aided diagnosis in medical imaging: historical review, current status and future potential," *Computerized medical imaging and graphics*, vol. 31, no. 4-5, pp. 198–211, 2007.

[7] X. Zhang, S. Qiu, M. Geng, and H. He, "Enhancing detection of ssveps for high-speed brain-computer interface with a siamese architecture," in *2021 IEEE International Conference on Bioinformatics and Biomedicine (BIBM)*. IEEE, 2021, pp. 1623–1627.

[8] F. D. Khameneh, S. Razavi, and M. Kamasak, "Automated segmentation of cell membranes to evaluate her2 status in whole slide images using a modified deep learning network," *Computers in biology and medicine*, vol. 110, pp. 164–174, 2019.

[9] J. Liu, Q. Zheng, X. Mu, Y. Zuo, B. Xu, Y. Jin, Y. Wang, H. Tian, Y. Yang, Q. Xue *et al.*, "Automated tumor proportion score analysis for pd-l1 (22c3) expression in lung squamous cell carcinoma," *Scientific Reports*, vol. 11, no. 1, p. 15907, 2021.

[10] S. Tewary, I. Arun, R. Ahmed, S. Chatterjee, and S. Mukhopadhyay, "Autoihc-analyzer: computer-assisted microscopy for automated membrane extraction/scoring in her2 molecular markers," *Journal of Microscopy*, vol. 281, no. 1, pp. 87–96, 2021.

[11] A. Brügmann, M. Eld, G. Lelkaitis, S. Nielsen, M. Grunkin, J. D. Hansen, N. T. Foged, and M. Vyberg, "Digital image analysis of membrane connectivity is a robust measure of her2 immunostains," *Breast cancer research and treatment*, vol. 132, pp. 41–49, 2012.

[12] C.-Y. Chang, Y.-C. Huang, and C.-C. Ko, "Automatic analysis of her-2/neu immunohistochemistry in breast cancer," in *2012 Third International Conference on Innovations in Bio-Inspired Computing and Applications*. IEEE, 2012, pp. 297–300.

[13] Y.-L. Kuo, C.-C. Ko, and J.-Y. Lai, "Automated assessment in her-2/neu immunohistochemical expression of breast cancer," in *2010 International Symposium on Computer, Communication, Control and Automation (3CA)*, vol. 2. IEEE, 2010, pp. 585–588.

[14] A. C. Ruifrok, D. A. Johnston *et al.*, "Quantification of histochemical staining by color deconvolution," *Analytical and quantitative cytology and histology*, vol. 23, no. 4, pp. 291–299, 2001.

[15] E. Ficarra, S. Di Cataldo, A. Acquaviva, and E. Macii, "Automated segmentation of cells with ihc membrane staining," *IEEE Transactions on Biomedical Engineering*, vol. 58, no. 5, pp. 1421–1429, 2011.

[16] F. D. Khameneh, S. Razavi, and M. Kamasak, "Automated segmentation of cell membranes to evaluate her2 status in whole slide images using a modified deep learning network," *Computers in Biology and Medicine*, vol. 110, pp. 164–174, 2019. [Online]. Available: https://www.sciencedirect.com/science/article/pii/S0010482519301878

[17] M. Saha and C. Chakraborty, "Her2net: A deep framework for semantic segmentation and classification of cell membranes and nuclei in breast cancer evaluation," *IEEE Transactions on Image Processing*, vol. 27, no. 5, pp. 2189–2200, 2018.

[18] S. Dimopoulos, C. E. Mayer, F. Rudolf, and J. Stelling, "Accurate cell segmentation in microscopy images using membrane patterns," *Bioinformatics*, vol. 30, no. 18, pp. 2644–2651, 2014.

[19] J.-Y. Zhu, T. Park, P. Isola, and A. A. Efros, "Unpaired image-to-image translation using cycle-consistent adversarial networks," in *Proceedings of the IEEE international conference on computer vision*, 2017, pp. 2223–2232.

[20] Y. Zhou, J. Huang, C. Wang, L. Song, and G. Yang, "Xnet: Wavelet-based low and high frequency fusion networks for fully-and semi-supervised semantic segmentation of biomedical images," in *Proceedings of the IEEE/CVF International Conference on Computer Vision*, 2023, pp. 21 085–21 096.

[21] F. Aurenhammer and R. Klein, "Voronoi diagrams." *Handbook of computational geometry*, vol. 5, no. 10, pp. 201–290, 2000.

[22] D. Zhang and D. Zhang, "Wavelet transform," *Fundamentals of image data mining: Analysis, Features, Classification and Retrieval*, pp. 35–44, 2019.

[23] O. Ronneberger, P. Fischer, and T. Brox, "U-net: Convolutional networks for biomedical image segmentation," in *Medical image computing and computer-assisted intervention–MICCAI 2015: 18th international conference, Munich, Germany, October 5-9, 2015, proceedings, part III 18*. Springer, 2015, pp. 234–241.

[24] Y. Ganin and V. Lempitsky, "Unsupervised domain adaptation by back-propagation," in *International conference on machine learning*. PMLR, 2015, pp. 1180–1189.

[25] I. Loshchilov and F. Hutter, "Decoupled weight decay regularization," *arXiv preprint arXiv:1711.05101*, 2017.

[26] P. Isola, J.-Y. Zhu, T. Zhou, and A. A. Efros, "Image-to-image translation with conditional adversarial networks," in *Proceedings of the IEEE conference on computer vision and pattern recognition*, 2017, pp. 1125–1134.

[27] S. Jha, R. Kumar, I. Priyadarshini, F. Smarandache, H. V. Long *et al.*, "Neutrosophic image segmentation with dice coefficients," *Measurement*, vol. 134, pp. 762–772, 2019.

[28] D. P. Huttenlocher, G. A. Klanderman, and W. J. Rucklidge, "Comparing images using the hausdorff distance," *IEEE Transactions on pattern analysis and machine intelligence*, vol. 15, no. 9, pp. 850–863, 1993.